Relationship between Shale Hydration and Shale Collapse

Wenxin Dong, Jian Tian,* Qiang Chen, Pengxiang Wang, Tao Han, Yufen Zhai, and Deyi Jiang

Read Online

ACCESS | Metrics & More | Article Recommendations

ABSTRACT: Shale gas has become the major source of natural gas. However, shale is rich in clay and easily collapsed by water invasion. This not only causes collapse of the reservoir but also causes the loss of natural gas and can even cause local earthquakes and affect the safety of human beings. This paper describes an investigation of the relationship between hydration and collapse. Shale samples were obtained from a series of wells drilled in the lower Silurian Longmaxi Formation at a depth of 3500 m. The different hydrated shales were simulated to analyze the hydration−collapse relationship. Magnetic resonance analysis and mechanical analysis were combined to analyze the collapse of the hydrated shales. The collapse progression was found to follow an S-shaped growth curve that can be divided into three parts, namely, the potential period, the exciting period, and the mature period. The hydration state and degree of damage were determined from the magnetic resonance of water molecules. This paper proposes a mechanism for shale hydration collapse based on basal and numerical data that can be used to predict shale collapse as a function of hydration.
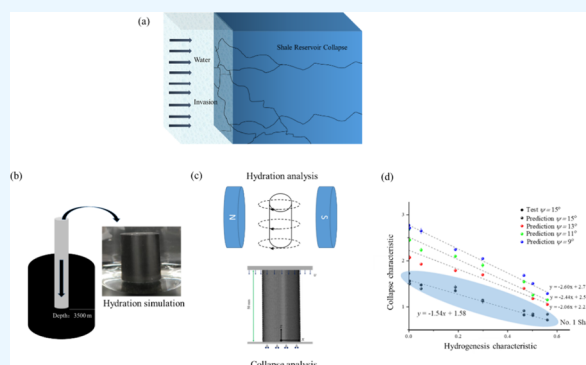
1. INTRODUCTION

As traditional energy sources are fully developed, shale gas reservoirs, an unconventional type of reservoir, have been deeply exploited, and shale gas has become the main source of natural gas.[1−4]

Beginning with the revolution in America in 2007 and continuing until 2015, the volume of research papers on shale gas grew explosively, and shale gas became a major focus of research interest in the fuel field (Figure 1). However, many accidents related to shale collapse occurred as more shale gas sites were developed.[5,6]

In recent years, thousands of research reports about shale collapses have been published. Chinese researchers have played an important role in this process, publishing numerous reports on the collapse of shale blocks due to water invasion. China's shale gas reservoirs are mainly distributed in the Xinjiang Basin and Sichuan Basin.[7−9]

The shale in the Sichuan Basin is rich in clay and can be easily hydrated, which is why it is vulnerable to collapse.[10,11] In a previous study, 82 marine shale samples were obtained from 10 evaluation wells drilled in the Wufeng−Longmaxi Formation in the southern Sichuan Basin of China and were used to explore the role of clay in shale hydration.[12] The results showed that clay minerals are carriers for water absorption because of their interlayer polarity and water wettability. Water activity was also shown to be a key factor in the failure mechanism of shale. Shale samples with higher clay contents had greater water activity.[10] The interaction of water

with shale can destabilize a wellbore and reduce the rate of gas production from a reservoir.[13]

Therefore, it is necessary to understand the relationship between the degree of hydration and the collapse of hydrated shale. In this study, low-field nuclear magnetic resonance (LFNMR) technology and uniaxial compression testing (UCT) were employed to explore the collapse behavior of hydrated shale.

2. THEORETICAL BASIS

2.1. Fundamental Principles of LFNMR. LFNMR has been widely applied in determining the degree of water saturation of animal tissues, wood, and rock.[14−18] In 2015, LFNMR was first employed by Washburn and Birdwell to analyze water in shale.[19] LFNMR has since been developed as an effective method for analyzing water in unconventional reservoirs. Nuclear magnetic resonance (NMR) is produced by simply releasing a radio-frequency (RF) field with the same frequency as 1H water, in which low-energy 1H jumps to a higher energy level, namely, the Zeeman transition.[20] 1H then gradually releases energy in a nonradiative manner. In the
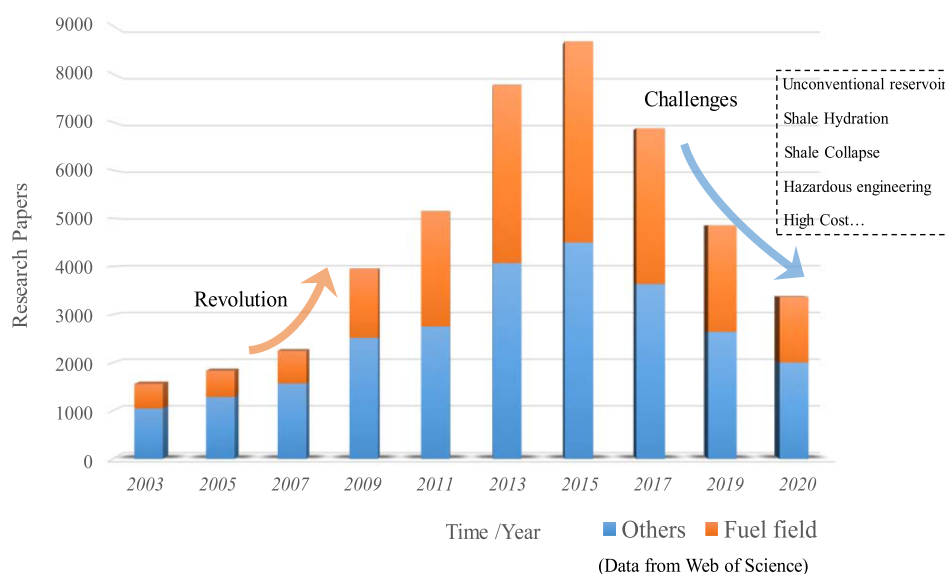
Figure 1. Global volume of research papers about shale from 2003 to 2020.

macroscopic horizon, transverse magnetization vectors move relative to each other, cut the coil, and induce an NMR signal that can be expressed as follows[21−23]

$$V(t) \propto M_z \ \sin\theta \ \cos(\omega_o t)e^{-t/T_2} \tag{1}$$

where M_z is the transverse magnetization vector at time t, θ is the cutting angle of the magnetization vector, ω_o is the angular velocity of the magnetization vector, and T_2 is the transversal relaxation time, which depends on the degree of freedom for water.

Obviously, the NMR signal is proportional to the amount of 1H water molecules at time T_2. The well-known T_2 spectrum can be generated from the machine inversion of the NMR signal. The degree of water saturation of the tested material can be calculated from the integral area of the T_2 spectrum and the T_2 value determined from the activity of the water. The T_2 spectrum can be further divided into bound water and free water components (Figure 2).
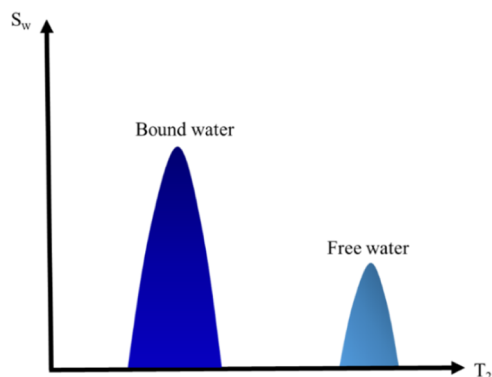

Figure 2. Bound and free water components of the T_2 spectrum.

2.2. Collapse Damage. Collapse damage was first proposed by Hillerborg et al. to describe concrete collapse under compressive loading. In 1989, Lubliner et al. described plastic damage as reflecting the nonlinear behavior and irreversible deformation that occur during the collapse process.[24] A series of modified plastic damage models

(PDM) has been developed to describe collapse behavior, including the elastic−plastic damage model (EDM), viscoelastic−plastic model (VM), and coupled elastoplastic damage model (CEDM).[25−27]

The onset of collapse behavior with increasing compressive stress is illustrated in Figure 3.
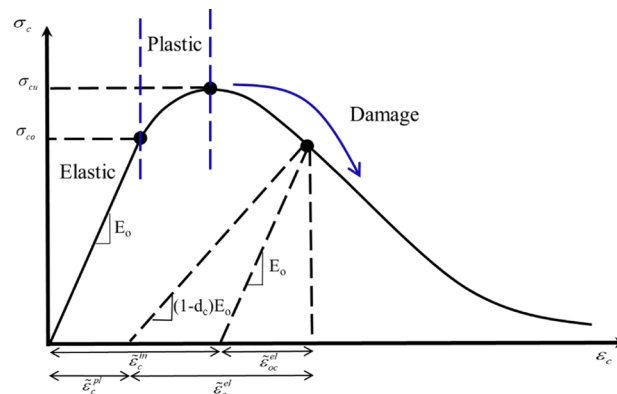

Figure 3. Collapse behavior in three-dimensional compression.

The stress−strain behavior shown in this figure can be divided into the elastic, plastic, and damage ranges, which involve four major components, namely, the yield criterion, hardening/softening law, damage evolution, and flow rule.

Normally, the normalized strain $\tilde{\varepsilon}$ can be decomposed into two parts according to the classical elastoplasticity theory

$$\tilde{\varepsilon}_c = \tilde{\varepsilon}_c^{pl} + \tilde{\varepsilon}_c^{el} \tag{2}$$

where $\tilde{\varepsilon}_c^{pl}$ and $\tilde{\varepsilon}_c^{el}$ are the plastic and elastic strain, respectively. A more general model for progressive material damage can be obtained by introducing a scalar damage variable d_c, $0 \leq d_c \leq 1$, as shown below

$$\sigma_c = (1 - d_c)E_o(\tilde{\varepsilon}_c - \tilde{\varepsilon}_c^{pl}) \tag{3}$$

where σ_c is the yield stress in compression and E_0 is the initial elastic stiffness of the material (prior to damage).
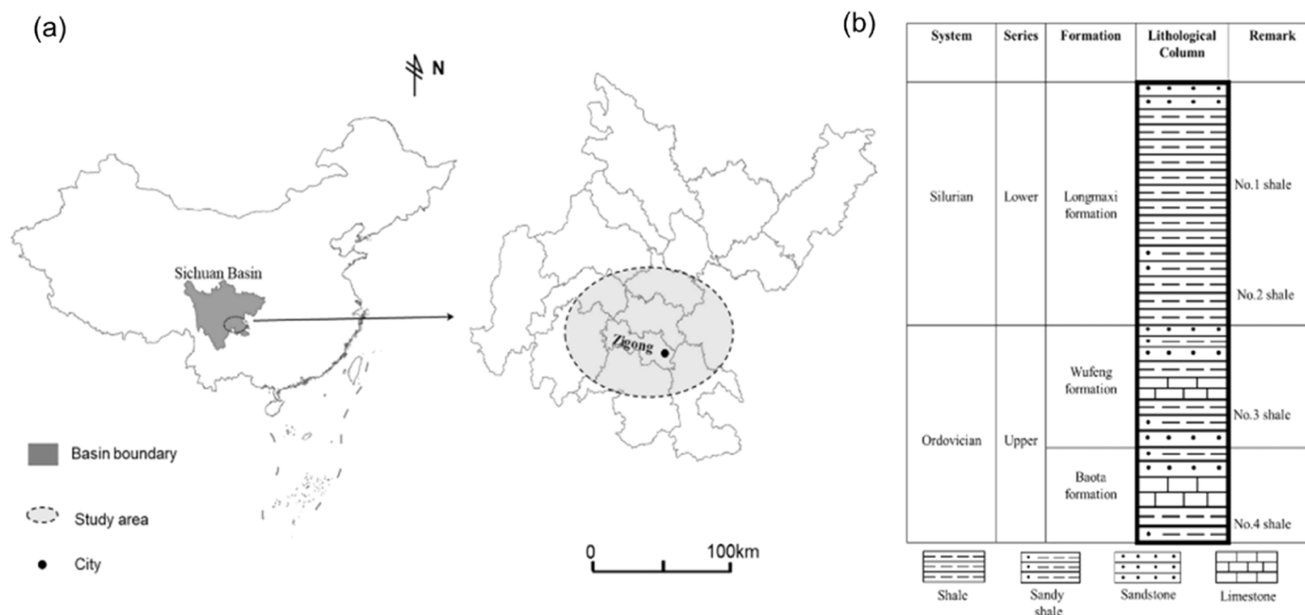
Figure 4. Geological setting of exploited shales. (a) Location of Sichuan shale field and (b) sedimentary sequences of shale measures in Zigong.

Table 1. Total Organic Carbon Contents and Mineral Compositions of Shale Samples

				mineral composition		
<!—Col Count:7F0E0samples	formation	R_0 (%)	total organic carbon (%)	clay	quartz	other
ZG1	Longmaxi	1.26	2.15	41.7	47.6	7.3
ZG2	Longmaxi	1.27	2.14	42.1	47.4	7.1
ZG3	Longmaxi	1.26	2.13	41.5	48.2	6.9
ZG4	Longmaxi	1.28	2.15	42.3	47.1	7.2
ZG5	Longmaxi	1.26	2.16	41.9	47.5	7.2
ZG6	Longmaxi	1.27	2.14	42.0	47.6	7.1
ZG7	Longmaxi	1.27	2.15	41.6	47.7	7.3
ZG8	Longmaxi	1.28	2.16	42.2	47.4	7.0
ZG9	Longmaxi	1.26	2.15	42.4	47.1	7.1

In describing the damage evolution, the normalized strain $\tilde{\varepsilon}$ can be refined further as follows

$$\tilde{\varepsilon}_c = \tilde{\varepsilon}_c^{in} + \tilde{\varepsilon}_{oc}^{el} \tag{4}$$

$$\tilde{\varepsilon}_{oc}^{el} = \frac{\sigma_c}{E_o} \tag{5}$$

where $\tilde{\varepsilon}_c^{in}$ is the inelastic strain and $\tilde{\varepsilon}_{oc}^{el}$ is the calculated elastic strain with respect to the original stiffness. The normalized plastic strain and damage can be expressed as follows

$$\tilde{\varepsilon}_c^{pl} = \tilde{\varepsilon}_c^{in} - \frac{d_c}{(1-d_c)}\frac{\sigma_c}{E_0} \tag{6}$$

$$d_c = \frac{(1-\beta)\tilde{\varepsilon}_c^{in}E_0}{\sigma_c + (1-\beta)\tilde{\varepsilon}_c^{in}E_0} \tag{7}$$

where β is the ratio of $\tilde{\varepsilon}_c^{pl}$ to $\tilde{\varepsilon}_c^{in}$. Therefore, the collapse damage can be calculated and predicted from the collapse curve.

3. EXPERIMENTS AND METHODS

3.1. Geological Setting. The Sichuan Basin, with a total area of approximately 260,000 sq km, is one of the major basins in China and is located in the southwest of China

(Figure 4a). In this study, the maximum diameter of the exploration zone was approximately 100 km. The Zigong shale field is located on the southeast boundary of the Sichuan Basin.

The sedimentary sequences in the Sichuan Basin were deposited in a mainly marine sedimentary environment (Figure 4b). Four shale exploration targets located in the upper Ordovician Wufeng and Baota Formations and the lower Silurian Longmaxi Formation were considered. The majority of the explored shales were complex, with inserting sandstone and limestone. The series of No. 1 shale is distributed continuously, with horizontal bedding at depths from 3200 to 3500 m. This suggests that the formation evolution of this period is complete.

3.2. Sample Preparation. In this study, nine shale samples were collected from the No. 1 shale in the Longmaxi Formation. The mineral compositions of the collected samples are shown in Table 1.

The average clay content was more than 40%, which illustrates that the drilled shale is typically water-sensitive shale that can be easily hydrated. The collected shale cores had diameters of 25 mm and heights of 50 mm.

To simulate different hydration situations, the shale cores were first soaked in 100% distilled water for different amounts of time. The hydrated shales were then subjected to further evaluation.
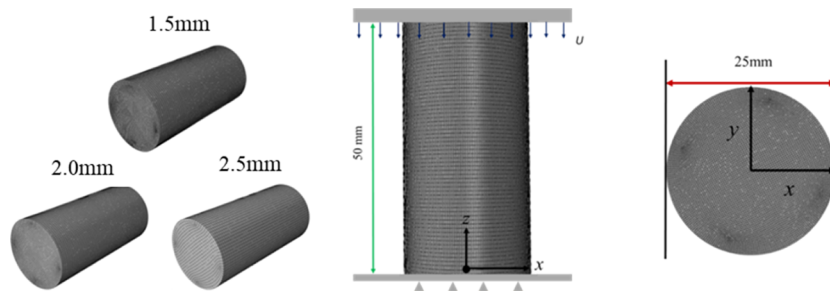
Figure 5. Specimens and numerical model for collapse behavior analysis.
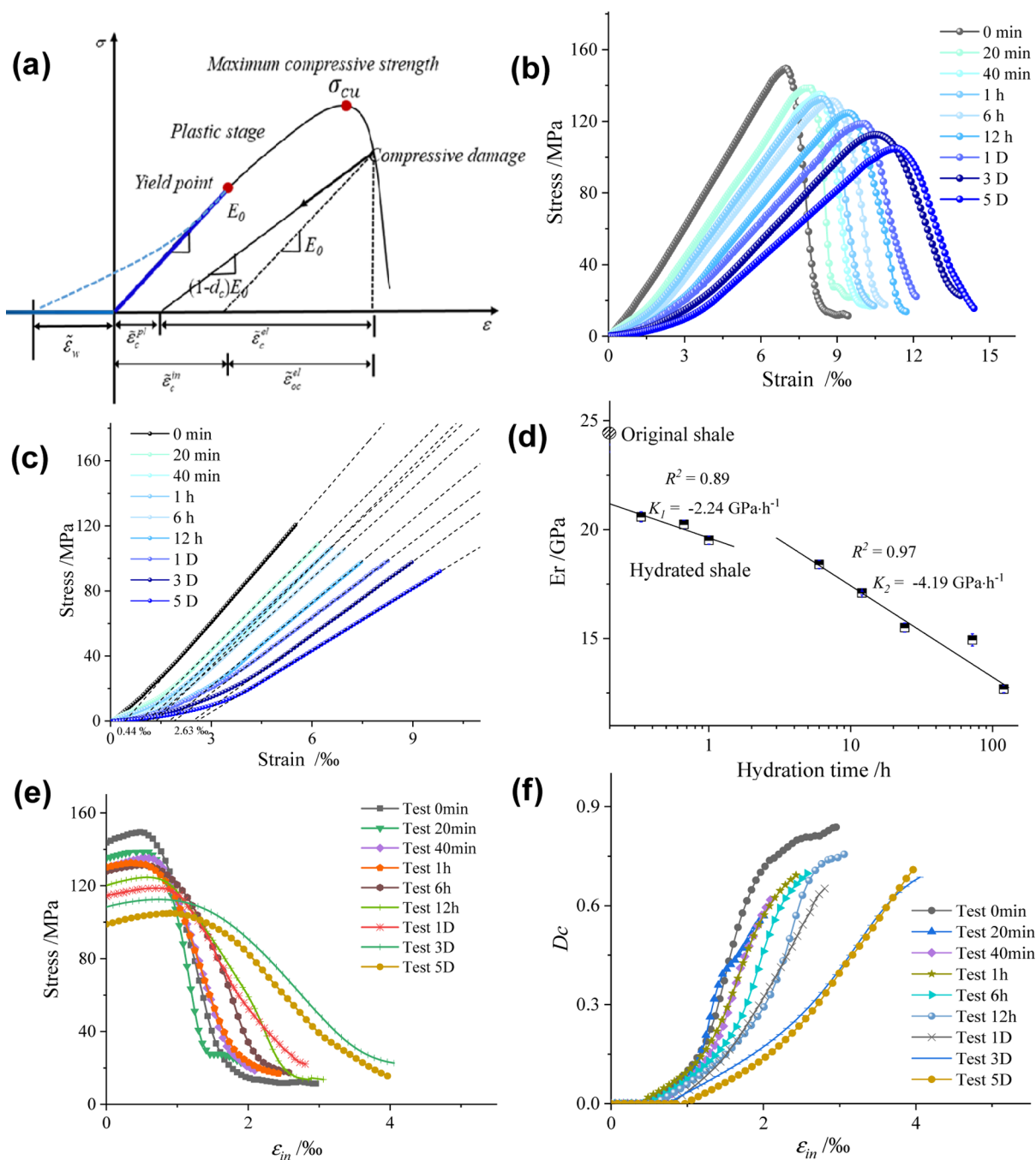

Figure 6. (a) Mechanism of collapse behavior of hydrated shale, (b) UCT test data for hydrated shale, (c) fitting curves of linear elasticity in the initial softening stage, (d) division of the real elastic modulus with hydration time, (e) change in compressive stress with inelastic deformation, and (f) evolution of collapse damage with increasing inelastic deformation.

3.3. LFNMR Analysis. The LFNMR technique is a lossless, in situ analysis technique that can be used to quickly determine the water content of a sample. Hydrated shale was placed into the sample cell of the NMR whole-core analysis system (version MiniMR60; Niumag, Shanghai; resonance frequency 23.1 MHz, magnet strength 0.5 T; probe coil 60 mm; experimental temperature range 31.99−32.00 °C) to obtain LFNMR T_2 spectra of the hydrated shale by calculating the integral area of the T_2 spectrum and substituting the value into eq 8

$$y = kx + b \qquad (8)$$

where x is the integral area of the T_2 spectrum, y is the water mass of the standard sample, k is the slope of the standard equation, and b is the vertical intercept of the standard equation.

The degree of water saturation of the hydrated shale can be obtained from eq 9.[28,29]

$$S_w = \frac{m_w}{m_s} \times 100\% \qquad (9)$$

where S_w is the degree of water saturation of the hydrated shale and m_w and m_s are the water mass and total mass of the hydrated shale, respectively.

3.4. Collapse Behavior Analysis. An advanced rock mechanics analysis system (GCTS, Tempe, AZ, USA) was employed to monitor the compression (stress) and displacement (strain) at a loading rate of 0.001 mm/s. The longitudinal strain was obtained by dividing the longitudinal displacement in the axial direction by the original diameter of the test specimen. Young's modulus and Poisson's ratio were determined from the slopes of the linear fits to the axial stress−axial strain and lateral strain−axial strain data, respectively.[30,31]

3.5. Finite Element Analysis. Based on the shale samples, numerical specimens and models were developed for collapse behavior analysis, as shown in Figure 5. The diameter of the cylindrical specimen was 25 mm, and the height was 50 mm. During the finite element analysis (FEA), the spatial displacement vectors of the cylinder bottom were defined as zero in the analysis steps, and compression was achieved by modeling displacement under loading at a rate of 0.001 mm/s.

The finite element type used was the cubic C3D8R cell, and the mesh sizes were 1.5, 2.0, and 2.5 mm. To model large deformations and nonlinear behavior, an explicit algorithm was used to describe the quasi-dynamic compression process.

In FEA, the softening law reflects the shape and location of the loaded surface, as well as its evolution after initial yielding, thereby defining the post-peak behavior during plastic flow.[32] The evolution is driven by the equivalent plastic strain, as indicated in eqs 6 and 7 above. Regardless of the influence of tension damage, the tensile strength was assumed to be 10 times greater than the compressive strength.

The direction and magnitude of plastic deformation were determined by the non-associated potential flow rule used. The potential function G has a Drucker−Prager-type hyperbolic form

$$G = \sqrt{(e\sigma_{t_0} \ \tan \psi)^2 + \overline{q}^2} - \overline{p} \ \tan \ \psi = 0 \qquad (10)$$

where ψ is the dilation angle measured in the $p-q$ plane, t_0 is the uniaxial tensile stress, e is the eccentricity that defines the rate at which the function approaches the asymptote, and $e = 0.1$ by default. Because of the continuity and smoothness, this

potential can enable the flow direction to be uniquely determined.

4. RESULTS AND DISCUSSION

4.1. Collapse Behavior of Hydrated Shales. The collapse behavior of hydrated shales can be divided into four stages, as shown in Figure 6a. In the initial stage, the apparent modulus of elasticity increases gradually with increasing loading stress (Figure 6b). Softening develops with increasing hydration time. Figure 6c illustrates the limit of the strain evolution in the softening stage. After 5 days of hydration, the nominal strain in the softening stage increased gradually from 0.44 to 2.63‰. After compaction, compression reveals the real elasticity modulus (E_r) and the linear relationship between strain and loading stress, as shown in Figure 6c.

In comparison with the original shale, the E_r value of the hydrated shale was reduced by 46.58% to 12.67 GPa. Figure 6d reveals the change in E_r values for different hydration times. The reduction in the modulus of hydrated shale can be divided further into two stages. In the primary stage, the modulus decreases slightly, at a rate of 2.24 GPa h^{-1}. The modulus decreases further with increasing hydration time, and the slope increases to 4.19 GPa h^{-1}, which reflects the maximum contribution of water invasion to softening.

As the loading stress increases further, the relationship changes from linear to nonlinear, which indicates the initiation of inelastic behavior. This is usually caused by microdamage and the development of microcracks. The corresponding inelastic strain can be further distinguished from the linear strain and can be calculated from the following equation

$$\varepsilon = \varepsilon_w + \varepsilon_{el} + \varepsilon_{in} \qquad (11)$$

where ε is the total compressive strain, ε_w is the softening evolution caused by water, ε_{el} is the elastic strain, and ε_{in} is the inelastic strain.

With increasing hydration time, the maximum compressive stress decreases to 36%, and the evolution proceeds at a decreasing rate. These results reflect the degradation of the structure of hydrated shales. The shale damage can be calculated as shown in eq 7. Figure 6e illustrates the damage evolution in compression with inelastic strain. From the yield point to the maximum compressive strength, the deformation of the shale is nominally considered to be plastic strain. Figure 6f illustrates the change in the collapse damage factor (dc) for different hydration times. The development of dc can be divided into three periods, namely, the latent, excitation, and stationary periods. Plastic deformation occurs during the latent period. In this period, there is no obvious damage generation in the shale structure; the damage is mainly related to the growth of micropores. In the excitation period, dc increases significantly with increasing inelastic strain. This period is characterized mainly by the generation of cracks and makes a major contribution to the shale collapse. In the final period, the hydrated shale completely loses its stiffness, and dc reaches a limit of approximately 0.6−0.9.

4.2. Numerical Reproduction of Shale Collapse. The initial compression of hydrated shale is quite different from that of original shale. Based on the compression results for the hydrated shales, the model was modified as shown in Figure 6a to reflect the contribution of water invasion. In the first step, the hyperelastic model was introduced to describe the initial nonlinear increase of the elasticity with water invasion. In Abaqus, the hyperelastic model is usually applied to describe
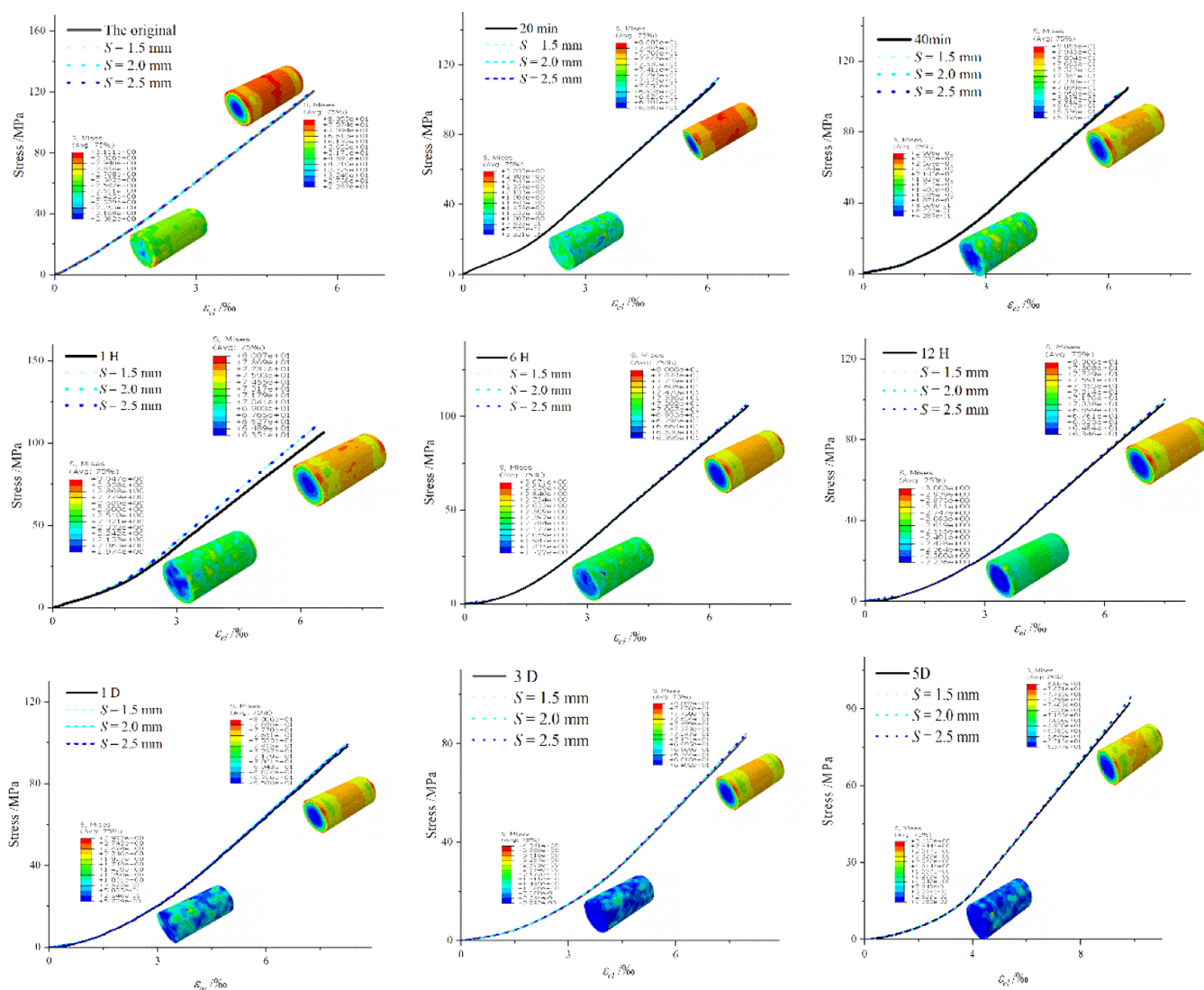
Figure 7. Finite element reproduction of nonlinear elastic behavior.

porous material which promises devolution with micropores between molecular chains, mineral layers, or solid particles.[33,34]

The Marlow model was used in this study to simulate hyperelastic behavior.[35] The Marlow model assumes that the strain energy potential is independent of the second deviatoric invariant. In the case of the Marlow model, the material coefficients can be calibrated by the Abaqus software from experimental stress–strain data. For n nominal stress–nominal strain data pairs, the relative error measure E is minimized

$$E = \sum_{i=1}^{n} \left(1 - T_i^{\text{th}} / T_i^{\text{test}}\right)^2 \tag{12}$$

where T_i^{test} is a stress value from the test data and T_i^{th} comes from one of the nominal stress expressions. During the simulation process, Abaqus minimizes the relative error rather than an absolute error measure since this provides a better fit at lower strains. Abaqus will also construct a strain energy potential and reproduce the test data exactly.

Based on this approach, the hyperelastic behavior of the hydrated shale was reproduced, as shown in Figure 7. All of the nonlinear elasticity was well reproduced. However, the initial axial stress distribution was not uniform in comparison with

the original shale. This illustrates the evolution of shale softening with increasing hydration.

The collapse behavior of hydrated shale varies with the plastic deformation, as shown in Figure 8a. According to eq 7, the plastic factor β is defined as the ratio of plastic strain to inelastic strain and is used to scale the dc and permit the reproduction of the failure curve. The numerical compressive behavior can reproduce the tested stress and inelasticity strain curves well, and the failure zones varied with the hydration time. With increasing hydration time, the initial inelastic strain increased from 0.42 to 1.05%, which indicates the development of a plastic zone with increasing hydration. The slope of the failure also decreased significantly with increasing hydration time, which reflects the transformation from brittle failure to plastic failure.

Figure 8b illustrates the numerical and tested evolution of collapse damage. The growth of dc can be divided into three stages. dc is initially defined as "0" in the absence of additional evolution of failure. This stage is mainly related to the growth of microcracks. In the next growth stage, the damage increases with increasing nominal inelastic strain and approaches a maximum. In the final stage, the hydrated shale loses its stiffness, and the damage reaches a maximum. In both test and
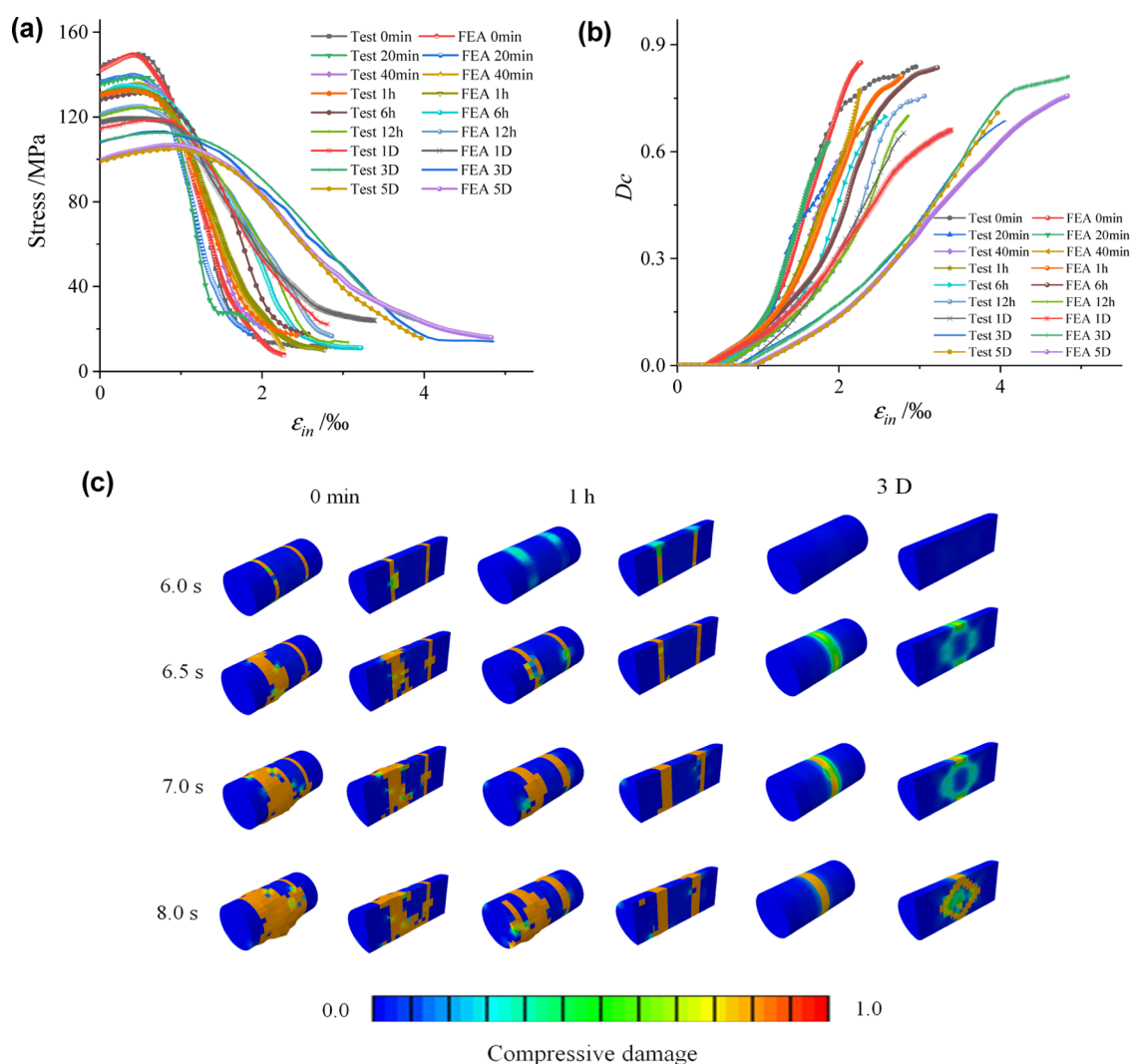
Figure 8. Numerical reproduction of shale collapse. (a) Numerical and tested compressive stress and inelastic strain curves of hydrated shales, (b) numerical and tested evolution of collapse damage and inelastic deformation of hydrated shales, and (c) FEA imaging of the evolution of shale collapsing process after 0, 1 h, or 3 days of hydration.

numerical results, the maximum decreases with increasing hydration time. This again reflects the transformation from brittle failure to plastic failure and slows the rate of release of fracture energy with increasing inelastic strain.

Figure 8c illustrates the process of hydrated shale collapse. During the confined simulation time, the majority of the original shale collapsed. At a simulation time of 6 s, cracking was primarily produced. Between 6.5 and 8.0 s, the cracks produced developed remarkably, became effectively cross-linked with each other, and gradually resulted in collapse. As the hydration time increased to 1 h, the generation of cracks was slow at the initial simulation timing. In comparison with the original shale, the damage in the FE body can be observed to have been reduced significantly. With further hydration, it becomes increasingly difficult to produce cracks, and the damage is further reduced. This indicates that hydration can delay crack generation because hydration increases the plastic zone and is conducive to plastic rather than brittle failure.

4.3. Numerical Prediction of Shale Collapse. Shale exhibits an unconventional layer bedding. The layer bedding angle determines the dilation angle. A shale layer loaded more closely parallel to the bedding exhibits a smaller dilation angle (typically 9°) than one loaded more normal to the bedding (typically 15°),[36] as shown in Figure 9.

Based on this observation, dilation angles from 9 to 15° were simulated to predict shale collapse for different bedding angles. The bedding of the tested shales was horizontal, and the dilation angle was defined at 15° (Figure 9). Different dilation angles were simulated by considering changes in the bedding structure. With decreasing dilation angle, the evolution of the failure was reduced, and the failure tended to be brittle. In a shale layer loaded parallel to the bedding, cracks are produced more easily. However, this brittle failure tendency can be changed with further hydration. Regardless of the dilation angle, the evolution of failure was obviously increased when the hydration time was increased to 5 days, and the brittle failure gradually changed to plastic failure. To better describe the transformation of the damage, the damage growth was further described by collapse curves. Figure 10 illustrates the damage growth of hydrated shales with different dilation angles. The damage growth was found to exhibit typical S-shape growth, which can be understood as being associated with the development of microcracks and micropores. An S
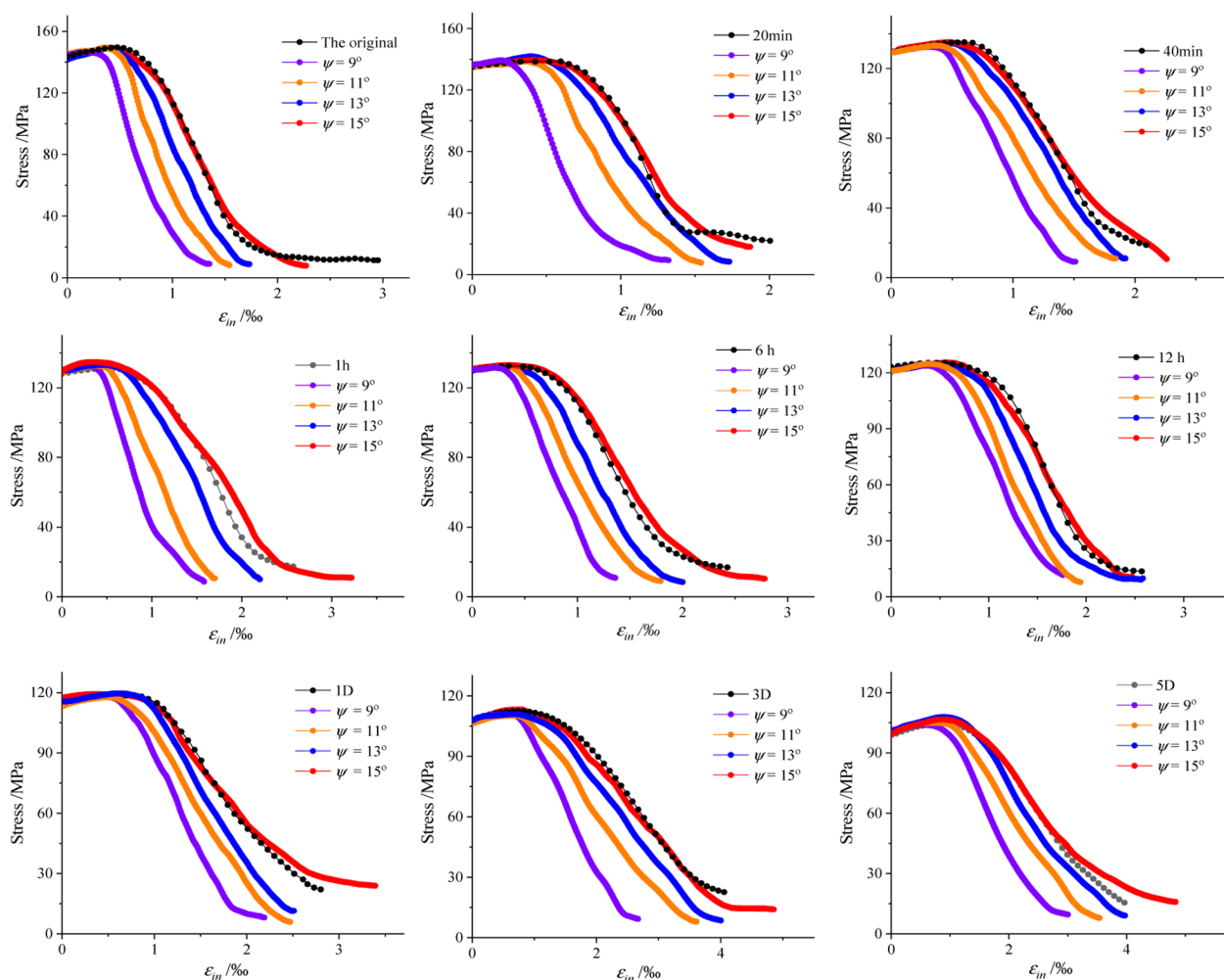
(a)
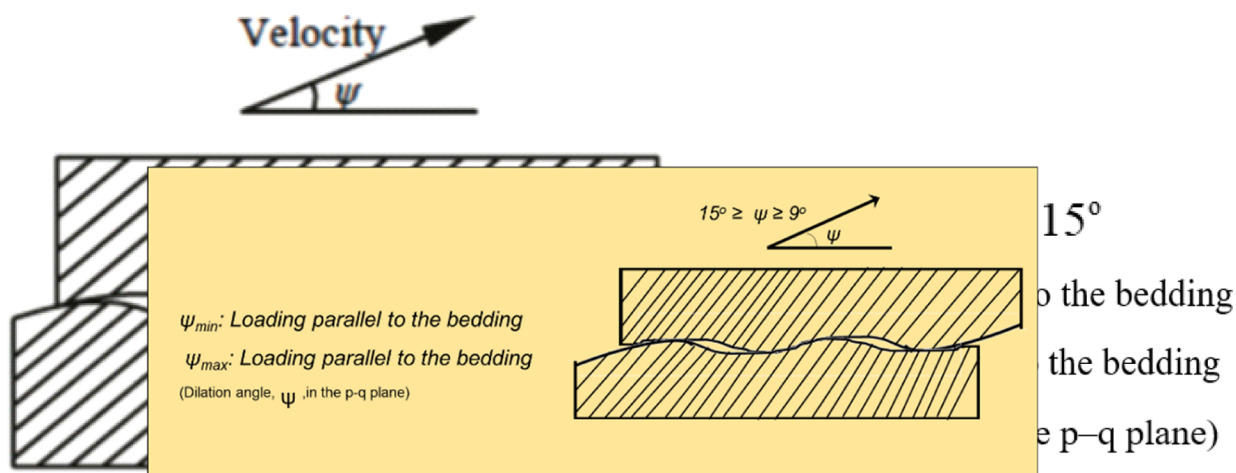
(b)

Figure 9. Prediction of the evolution of collapse damage for different bedding angles.

Gompertz (SG) growth model was employed to model the damage growth.[37,38]

According to the basal data, predicted values were obtained for the maximum damage ($a = 1.0$). A 90% confidence interval and 90% prediction interval were also determined. The intervals gradually increase in width with increasing hydration time. The growth can be divided into three parts, namely, potential period, excited period, and mature period. With

increasing hydration time, the potential period is expanded, and it expands further with increasing dilation angle. In comparison with the results for the minimum dilation angle ($\psi = 9°$), dilation angles of $\psi = 11°$, $\psi = 13°$, and $\psi = 15°$ expanded the potential period by 16.3, 31.8, and 37.5%, respectively. In the exciting period, the damage tended to grow linearly. The first derivative at the midpoint was used to evaluate the growth during the exciting period. According to
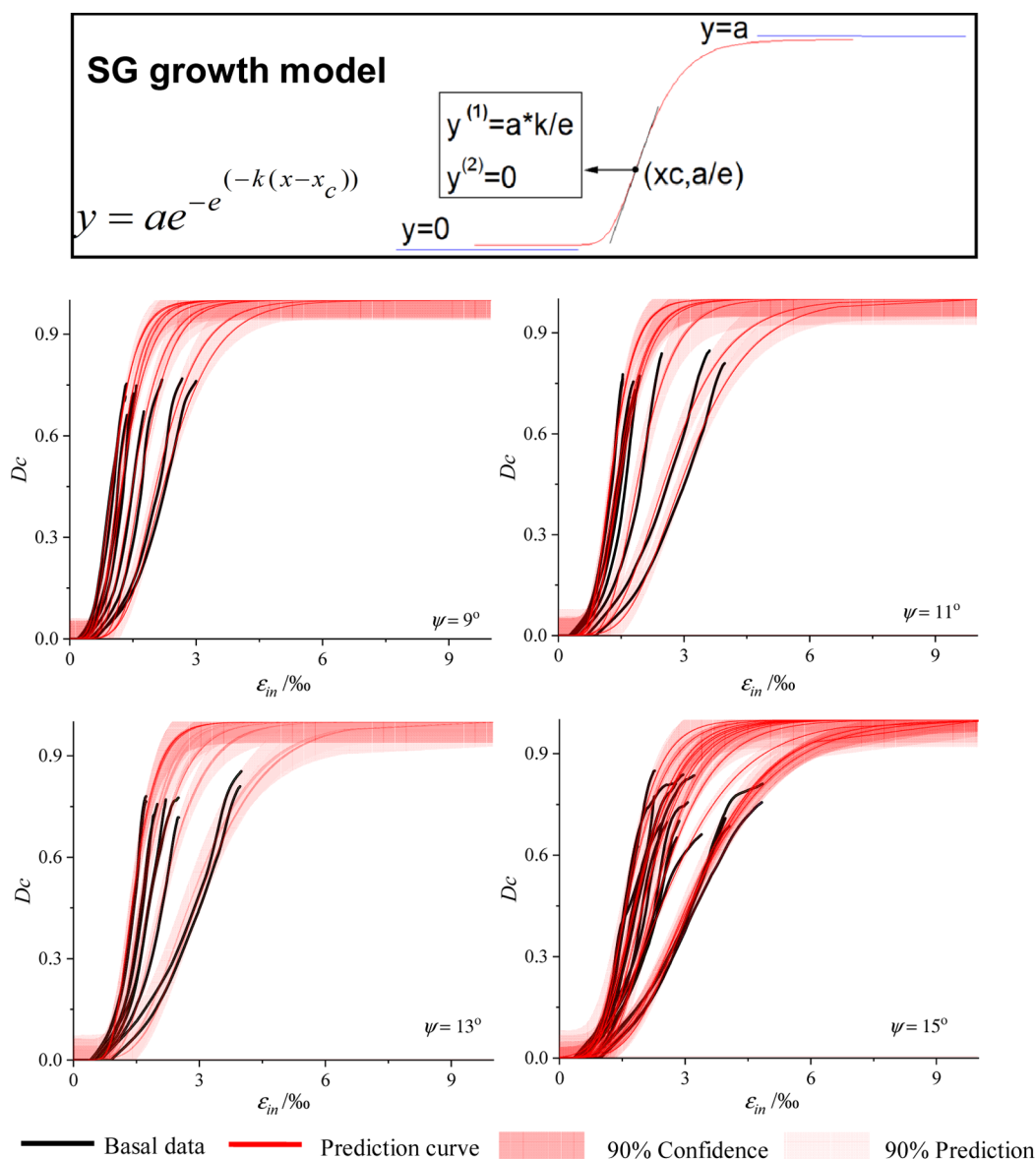
Figure 10. Collapse damage growth prediction for different bedding angles.

the SG model, the slope can be simply expressed by a constant K value. The value of K decreases with increasing hydration time. This can be easily understood as reflecting the increasing hydration damage.

4.4. Analysis of the Hydration Damage of Hydrated Shales. Figure 11 shows the water content of shale at different times. In the initial stage ($t = 20$ min), the total saturation of shale was 0.57%, and the degrees of bound water and free water saturation were 0.52 and 0.05%, respectively. The T_2 distribution of bound water was not completely separated from the T_2 distribution of free water. This is consistent with the capillary theory. Adsorbed water permeates into extremely small pores. However, the T_2 distributions of bound water and free water were not completely separate. The small pores in shale should not be completely saturated, according to the T_2 hump. The free water outside the pores is available for subsequent invasion.

During the next 1 h of hydration, the measured T_2 peak increased slightly, and the continuous hump still existed. The total saturation of shale at a hydration time of 40 min increased

to 0.34%. These results indicate that a long process is involved in saturating extremely small pores during the initial stage. After the shale was hydrated for 1 h, the total saturation increased significantly to 5.17%, and the T_2 distribution of the free water shifted to the right. Furthermore, the saturation associated with the contribution of bound water increased 18.52−0.64% when the hydration time increased to 6 h. The T_2 distribution of free water was first separated from that of bound water. This indicates that the majority of pores were saturated and that more water would be removable because of the development of pores with hydration damage. When the shale was hydrated for more than 24 h, the saturation of bound water increased significantly to 1.01%, and the peak of the free water moved to the right, which indicates further damage to shale pores and causes the free water to move.

With further increases in hydration time, there were no obvious changes in the free water saturation. However, the saturation of bound water continued to increase and eventually increases by 21.50% from day 1 to day 5, which indicates that the further hydration was mainly caused by the bound water.
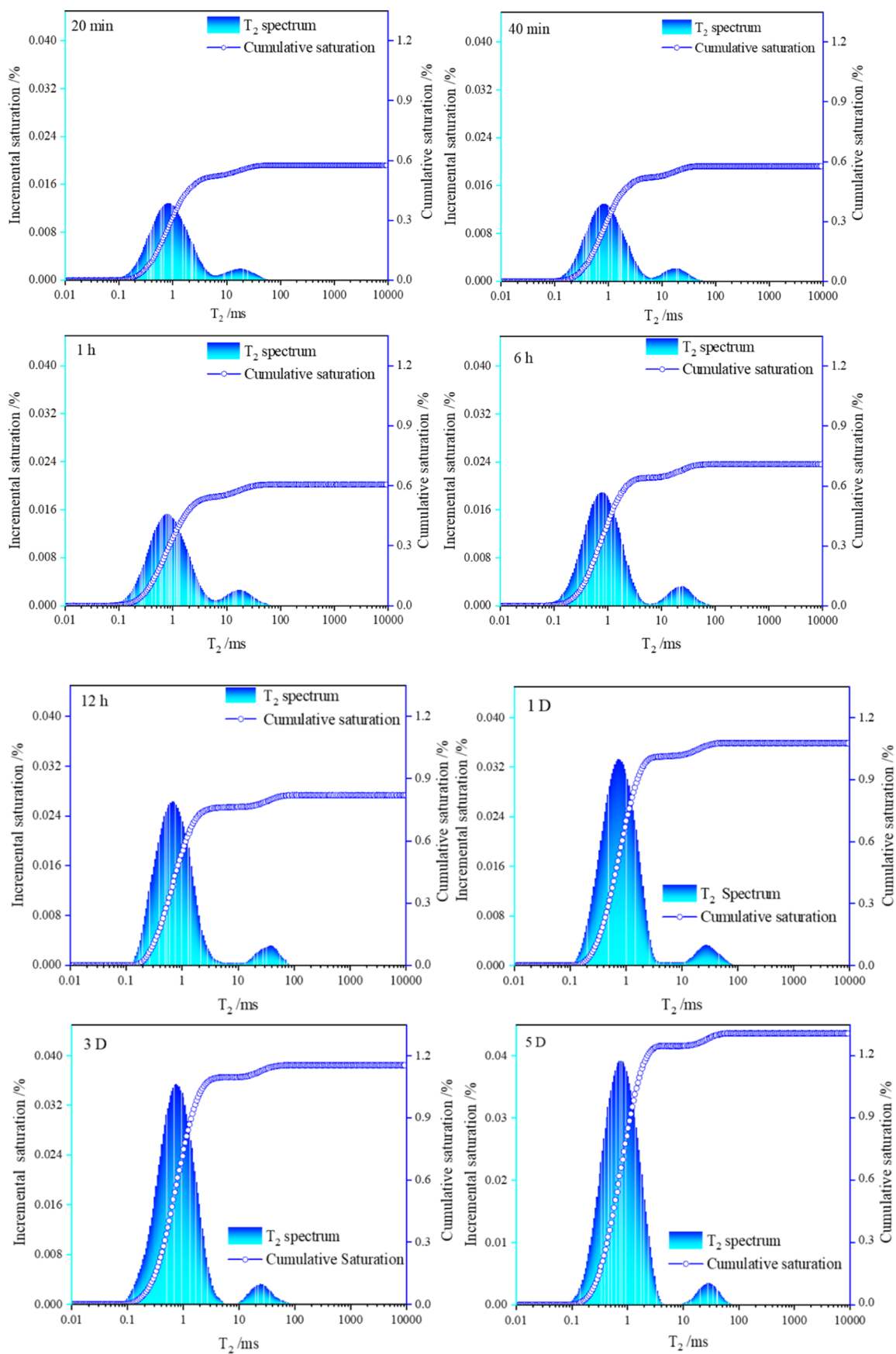
Figure 11. T_2 distributions of hydrated shales at different T_2 times.

The continuous increase in the bound water also indicates the growth of pores.

For the growth of pores, the generation of microcracks can be described by a density function $n(r,t)$, which indicates the number of cracks in the scale of Δr at time t. In the initial stage of damage, ignoring the correlation between cracks, the evolution of n is mainly determined by nucleation and crack propagation. The evolution of n can be derived from the following equations.

The change in microcrack density in an r to $r + \Delta r$ phase element of a one-dimensional phase space can be expressed as follows

$$\int_r^{r+\Delta r} n(r,\, t) \mathrm{d}r$$

The change over an increment of time Δt can be expressed as follows

$$\int_r^{r+\Delta r} [n(r,\, t + \Delta t) - n(r,\, t)] \mathrm{d}r$$

This can be divided into two parts as follows

$$\int_t^{t+\Delta t} \mathrm{d}t \int_r^{r+\Delta r} n_{\mathrm{N}}(r,\, t) \mathrm{d}r$$

which represents the source term of microcracks in the phase element. n_{N} represents the density of nucleation rate. The flow generated by crack propagation can be further divided into inflow and outflow

$$\int_r^{r+\Delta r} \mathrm{d}r [n(r,\, t) \dot{r}(r,\, t) - n(r + \Delta r,\, t) \dot{r}(r + \Delta r,\, t)]$$

where $\dot{r}$ is the rate of crack propagation.

Assuming that Δt and Δr tended to be zero, the evolution of crack density can be simplified as follows

$$\frac{\partial n}{\partial t} + \frac{\partial (\dot{r} n)}{\partial r} = n_{\mathrm{N}} \tag{13}$$

In this way, we can describe the evolution of n in terms of r and n_{N}.

According to the above equations, the relaxation time of water in the pores is related to the size of the pore space. As the pores become smaller, the surface area becomes larger, the effect of surface interaction becomes stronger, and T_2 becomes smaller. Therefore, the T_2 distribution can be used to evaluate the r value, and each T_2 corresponds to a certain r value.

The damage factor D can be described as follows

$$D = \int_0^{\infty} r n(t,\, r) \mathrm{d}r \tag{14}$$

According to the relationship between T_2 and the pore size r, the hydration process can be described in terms of the pore growth by the following equation

$$\frac{1}{T_2} \approx \rho \left(\frac{S}{V} \right) = F_s \frac{\rho}{r} \tag{15}$$

Here, ρ is the relaxation intensity at the surface, S/V is the ratio of pore surface area to pore volume, and F_s is a geometric factor. For spherical pores, F_s is equal to 3.0; for cylindrical passages, F_s is equal to 2.0.

Based on this, r can be replaced with T_2, and the damage factor D can be described in terms of T_2

$$D = \int_{T_0}^{T_2} F_s T_2 n(t,\, T_2) \mathrm{d}T_2 \tag{16}$$

According to the T_2 spectrum, the area of microdamage extension in Δt time can be described in terms of the T_2 integral area

$$S \approx \int F_s n(t,\, T_2) \mathrm{d}T_2 \tag{17}$$

Therefore, the damage equation can be expressed as follows

$$D_{\mathrm{T}} = \frac{S_{T_2} - S_{T_0}}{S_{T_2}} = 1 - \frac{S_{T_0}}{S_{T_2}} \tag{18}$$

Here, S_{T_0} is the integral area of the LFNMR peak at the initial hydration damage, and S_{T_2} is the integral area at time T_2.

However, it is difficult to choose the starting hydration as reflecting the initial hydration damage. The pores of shales are extremely small, and outside water needs a long time to invade. Therefore, we simply defined the starting test ($t = 20$ min) as corresponding to the initial hydration damage. Figure 12 shows
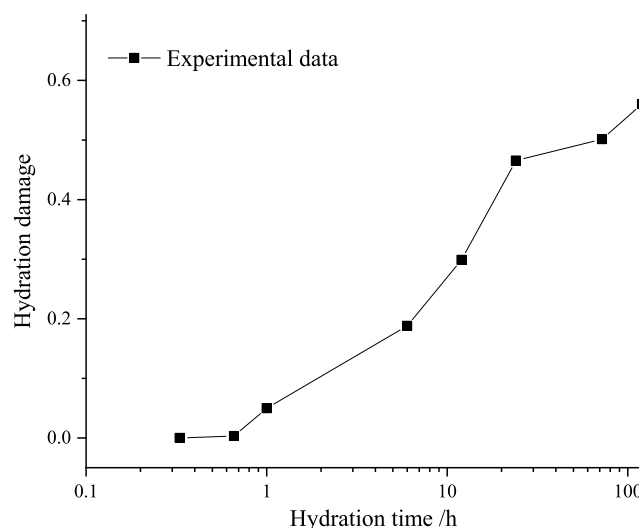

Figure 12. Development of hydration damage with hydration time.

the change in hydration damage with hydration time. The development of hydration damage can be described in three parts, namely, the potential stage, the growth stage, and the development stage. In the potential stage, there is no obvious development of damage during 40 min of hydration. With increasing hydration time, the hydration damage increases significantly from 40 min to 3 days. After 3 days of hydration, the damage develops further. This is attributable to crack growth.

4.5. Relationship between Hydration Damage and Collapse Damage. As mentioned above, collapse damage is strictly related to the structure parameter K. Figure 13 shows that the relation of K to the degree of hydration damage tends to be linear.

The results of this study demonstrate that the structure parameter is linearly related to damage and that lower and upper limits of the $K-D_t$ relation vary with the dilation angle. For hydrated shales, the linear slope of the relation increases with the increasing dilation angle. Considering the bedding structure of the Longmaxi Formation, the dilation angle of No.
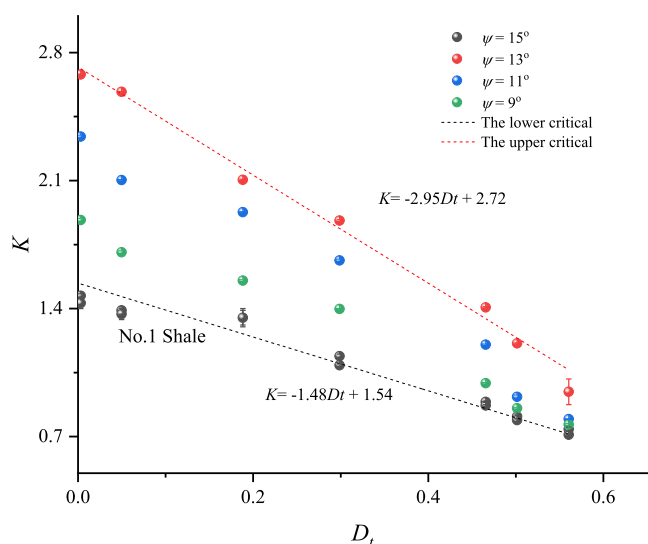
Figure 13. Critical K values of hydrated shales.

1 shale was considered to be 9°, and the predicted K values were consistent with the test data. The correlation coefficient was greater than 0.95. Based on the SG model, the following equation for hydration collapse as a function of hydration damage is proposed for No. 1 shale

$$D_C = e^{-e^{((1.48D_t - 1.54)(\varepsilon_{in} - 2.40D_t - 1.58))}} \tag{19}$$

where D_C is the collapse damage of the hydrated shale, D_t is the hydration damage, and ε_{in} is the inelastic strain during shale collapse. Hydration damage is the reason for the collapse. If the hydration damage can be measured, potential collapse damage can be easily predicted, and the collapse process beyond the elastic zone can be simulated. Some protective measures can then be applied in the case of water invasion.

5. CONCLUSIONS

By combining LFNMR and UCT measurements, the collapse of hydrated shales was interpreted from the magnetic resonance of water molecules, and the relationship between shale hydration and collapse was investigated. An SG growth model was developed to describe damage progression in hydrated shale. Different numerical dilation models were compared to the proposed collapse model in terms of fitting performance. The relationship between collapse damage and the dilation angle was also studied. We can draw the following conclusions from the results of this study:

1. Water invasion can result in the collapse of water-sensitive shale.
2. The damage growth model developed in this study fits the collapse curves and reflects the increasing degree of damage with increasing hydration time.
3. The hydration damage growth model was found to be applicable to different dilation angles, and the dilation angle was found to influence the duration of the exciting period.
4. The proposed hydration collapse model can be used to predict the potential collapse of hydrated shales as a function of the degree of hydration.

■ AUTHOR INFORMATION

Corresponding Author
Jian Tian − *State Key Laboratory of Coal Mine Disaster Dynamics and Control, Chongqing University, Chongqing 400044, China*; Email: tianjian2171@cqu.edu.cn

Authors
Wenxin Dong − *State Key Laboratory of Coal Mine Disaster Dynamics and Control, Chongqing University, Chongqing 400044, China; Sichuan Xinlin New Material Technology Company Limited, Zigong 643099, China; Jinsha Mining Technology (Chongqing) Company Limited, Chongqing 400030, China;* orcid.org/0000-0002-9555-7068
Qiang Chen − *State Key Laboratory of Coal Mine Disaster Dynamics and Control, Chongqing University, Chongqing 400044, China;* orcid.org/0000-0002-4727-7520
Pengxiang Wang − *Downhole Service Company, CNPC Chuanqing Drilling Engineering Company Limited, Chengdu 610051, China*
Tao Han − *Chongqing Optoelectronics Research Institute, Chongqing 400060, China*
Yufen Zhai − *Jianghan Oilfield Oil Production Plant, SINOPEC Jianghan Oilfield Company Limited, Qianjiang 433124, China*
Deyi Jiang − *State Key Laboratory of Coal Mine Disaster Dynamics and Control, Chongqing University, Chongqing 400044, China*

Complete contact information is available at:
https://pubs.acs.org/10.1021/acsomega.2c04852

Notes
The authors declare no competing financial interest.

■ REFERENCES
(1) Singh, P.; Slatt, R.; Borges, G.; et al. Reservoir Characterization of Unconventional Gas Shale Reservoirs: Example From the Barnett Shale, Texas, U.S.A. *Earth Sci. Res. J.* **2009**, *60*, 15−31.
(2) Vidic, R. D.; Brantley, S. L.; Vandenbossche, J. M.; Yoxtheimer, D.; Abad, J. D. Impact of Shale Gas Development on Regional Water Quality. *Science* **2013**, *340*, 1235009.
(3) Vengosh, A.; Jackson, R. B.; Warner, N.; Darrah, T. H.; Kondash, A. A critical review of the risks to water resources from unconventional shale gas development and hydraulic fracturing in the United States. *Environ. Sci. Technol.* **2014**, *48*, 8334−8348.
(4) Chen, S.; Zhu, Y.; Wang, H.; Liu, H.; Wei, W.; Fang, J. Shale gas reservoir characterisation: A typical case in the southern Sichuan Basin of China. *Energy* **2011**, *36*, 6609−6616.
(5) Ma, J.; Pang, S.; Zhou, W.; Xia, B.; An, Y. Novel Deep Eutectic Solvents for Stabilizing Clay and Inhibiting Shale Hydration. *Energy Fuels* **20212021**, *35*, 7833−7843.
(6) Liu, H.; Cui, S.; Meng, Y.; Li, Z.; Yu, X.; Sun, H.; Zhou, Y.; Luo, Y. Rock Mechanics and Wellbore Stability of Deep Shale During Drilling and Completion Processes. *J. Petrol. Sci. Eng.* **2021**, *205*, 108882.
(7) Wu, J. J.; Liu, L. C.; Zhao, G. H.; Chu, X. S. Research and Exploration of High Energy Gas Fracturing Stimulation Integrated Technology in Chinese Shale Gas Reservoir. *Adv. Mater. Res.* **2012**, *524−527*, 1532−1536.
(8) Wu, Y.; Cheng, L.; Huang, S.; Jia, P.; Zhang, J.; Lan, X.; Huang, H. A practical method for production data analysis from multistage

fractured horizontal wells in shale gas reservoirs. *Fuel* **2016**, *186*, 821−829.

(9) Wang, L.; Dong, Y.; Zhang, Q.; Duan, R. Numerical simulation of pressure evolution and migration of hydraulic fracturing fluids in the shale gas reservoirs of Sichuan Basin, China. *J. Hydrol.* **2020**, *588*, 125082.

(10) Wen, H.; Chen, M.; Jin, Y.; Zhang, Y.; Ge, W.; Du, J.; Zeng, C. Water activity characteristics of deep brittle shale from Southwest China. *Appl. Clay Sci.* **2015**, *108*, 165−172.

(11) Ma, Y.; Zhong, N.; Li, D.; Pan, Z.; Cheng, L.; Liu, K. Organic matter/clay mineral intergranular pores in the Lower Cambrian Lujiaping Shale in the north-eastern part of the upper Yangtze area, China: A possible microscopic mechanism for gas preservation - ScienceDirect. *Int. J. Coal Geol.* **2015**, *137*, 38−54.

(12) Wang, H.; Zhou, S.; Zhang, J.; Feng, Z.; Jiao, P.; Zhang, L.; Zhang, Q. Clarifying the Effect of Clay Minerals on Methane Adsorption Capacity of Marine Shales in Sichuan Basin, China. *Energies* **2021**, *14*, 6836.

(13) Yuan, W.; Li, X.; Pan, Z.; Connell, L. D.; Li, S.; He, J. Experimental Investigation of Interactions between Water and a Lower Silurian Chinese Shale. *Energy Fuels* **2014**, *28*, 4925−4933.

(14) Sánchez-Alonso, I.; Moreno, P.; Careche, M. Low field nuclear magnetic resonance (LF-NMR) relaxometry in hake (Merluccius merluccius, L.) muscle after different freezing and storage conditions. *Food Chem.* **2014**, *153*, 250−257.

(15) Li, M.; Wang, H.; Zhao, G.; Qiao, M.; Li, M.; Sun, L.; Gao, X.; Zhang, J. Determining the drying degree and quality of chicken jerky by LF-NMR. *J. Food Eng.* **2014**, *139*, 43−49.

(16) Al-Habsi, N. A.; Al-Hadhrami, S.; Al-Kasbi, H.; Rahman, M. S. Molecular mobility of fish flesh measured by low-field nuclear magnetic resonance (LF-NMR) relaxation: effects of freeze-thaw cycles. *Fish. Sci.* **2017**, *83*, 845−851.

(17) Cai, C.; Javed, M. A.; Komulainen, S.; Telkki, V.-V.; Haapala, A.; Heräjärvi, H. Effect of natural weathering on water absorption and pore size distribution in thermally modified wood determined by nuclear magnetic resonance. *Cellulose* **2020**, *27*, 4235−4247.

(18) Jiang, Y.; Xu, G.; Bi, H.; Shi, Y.; Gao, Y.; Han, X.; Zeng, X. A new method to determine surface relaxivity of tight sandstone cores based on LF-NMR and high-speed centrifugation measurements. *J. Petrol. Sci. Eng.* **2021**, *196*, 108096.

(19) Washburn, K. E.; Birdwell, J. E.A New Laboratory Approach to Shale Analysis Using NMR Relaxometry; *Unconventional Resources Technology Conference*, 2013; pp 1775−1782.

(20) Yao, Y.; Liu, D. Comparison of low-field NMR and mercury intrusion porosimetry in characterizing pore size distributions of coals. *Fuel* **2012**, *95*, 152−158.

(21) Mateus, M. L.; Champion, D.; Liardon, R.; Voilley, A. Characterization of water mobility in dry and wetted roasted coffee using low-field proton nuclear magnetic resonance. *J. Food Eng.* **2007**, *81*, 572−579.

(22) Straadt, I. K.; Thybo, A. K.; Bertram, H. C. NaCl-induced changes in structure and water mobility in potato tissue as determined by CLSM and LF-NMR. *LWT—Food Sci. Technol.* **2008**, *41*, 1493−1500.

(23) Lin, S.; Yang, S.; Li, X.; Chen, F.; Zhang, M. Dynamics of water mobility and distribution in soybean antioxidant peptide powders monitored by LF-NMR. *Food Chem.* **2016**, *199*, 280.

(24) Lubliner, J.Some Simple Models of Generalized Plasticity. *Advances in Plasticity*; Pergamon, 1989; pp 637−641.

(25) Xue, L.; Belytschko, T. Fast methods for determining instabilities of elastic−plastic damage models through closed-form expressions. *Int. J. Numer. Methods Eng.* **2010**, *84*, 1490−1518.

(26) Wrobel, M.; Papanastasiou, P.; Peck, D. A simplified modelling of hydraulic fractures in elasto-plastic materials. *Int. J. Fract.* **2022**, *233*, 153−178.

(27) Salari, M. R.; Saeb, S.; Willam, K. J.; Patchet, S. J.; Carrasco, R. C. A coupled elastoplastic damage model for geomaterials. *Comput. Methods Appl. Mech. Eng.* **2004**, *193*, 2625−2643.

(28) Guo, L. Y.; Shao, J. H.; Liu, D. Y.; Xu, X.-L.; Zhou, G.-H. The Distribution of Water in Pork Meat during Wet-curing as Studied by Low-field NMR. *Food Sci. Technol. Int.* **2014**, *20*, 393−399.

(29) Yuan, Y.; Rezaee, R. Fractal analysis of the pore structure for clay bound water and potential gas storage in shales based on NMR and N2 gas adsorption[J]. *J. Petrol. Sci. Eng.* **2019**, *177*, 756−765.

(30) Li, X.; Zhang, D.; Yu, G.; Li, H.; Xiao, W. Research on Damage and Acoustic Emission Properties of Rock Under Uniaxial Compression. *Geotech. Geol. Eng.* **2021**, *39*, 3549−3562.

(31) Zhong, Z.; Deng, R.; Zhang, J. Fracture properties of jointed rock infilled with mortar under uniaxial compression. *Eng. Fract. Mech.* **2020**, *228*, 106822.

(32) Nevitt, J. M.; Pollard, D. D.; Warren, J. M.New constraints on the rheology of granitic rock during faulting at the brittle-ductile transition: field observations, microstructural analysis and mechanical modeling. *AGU Fall Meeting Abstracts*, 2012; p T13E-2662.

(33) Franus, A.; Jemioło, S.; Antoni, A. M. A slightly compressible hyperelastic material model implementation in ABAQUS. *Eng. Solid Mech.* **2020**, *8*, 365−380.

(34) Peng, F.; Huang, W.; Zhang, Z. Q.; Fu Guo, T. F.; Ma, Y. E. Phase field simulation for fracture behavior of hyperelastic material at large deformation based on edge-based smoothed finite element method. *Eng. Fract. Mech.* **2020**, *238*, 107233.

(35) Pal, S.; Naskar, K. Machine Learning Model Predict Stress-Strain Plot for Marlow Hyperelastic Material Design. *Mater. Today Commun.* **2021**, *27*, 102213.

(36) Langhi, L.; Zhang, Y.; Gartrell, A.; Underschultz, J.; Dewhurst, D. Evaluating hydrocarbon trap integrity during fault reactivation using geomechanical three-dimensional modeling: An example from the Timor Sea, Australia. *AAPG Bull.* **2010**, *94*, 567−591.

(37) Shamurad, B.; Gray, N.; Petropoulos, E.; Tabraiz, S.; Membere, E.; Sallis, P. Predicting the effects of integrating mineral wastes in anaerobic digestion of OFMSW using first-order and Gompertz models from biomethane potential assays. *Renewable Energy* **2020**, *152*, 308−319.

(38) Conde-Gutiérrez, R. A.; Colorado, D.; Hernández-Bautista, S. L. Comparison of an artificial neural network and Gompertz model for predicting the dynamics of deaths from COVID-19 in México. *Nonlinear Dynam.* **2021**, *104*, 4655−4669.